Sulfated fibrous ZrO_2/Al_2O_3 core and shell nanocomposites: a novel strong acid catalyst with hierarchically macro-mesoporous nanostructure

Erming Liu, Ashley J. Locke, Ray L. Frost• and Wayde N. Martens

Discipline of Chemistry, Faculty of Science and Technology, Queensland University of Technology, GPO Box 2434, Brisbane Queensland 4001, Australia

ABSTRACT

A series of solid strong acid catalysts were synthesised from fibrous ZrO_2/Al_2O_3 core and shell nanocomposites. In this series, the zirconium molar percentage was varied from 2 % to 50 %. The ZrO_2/Al_2O_3 nanocomposites and their solid strong acid counterparts were characterised by a variety of techniques including ^{27}Al magic angle spinning nuclear magnetic resonance (MAS-NMR), scanned electronic microscopy (SEM), transmission electron microscope (TEM), X-ray photoelectron spectroscopy (XPS), Nitrogen adsorption and infrared emission spectroscopy (IES). NMR results show that the interaction between zirconia species and alumina strongly correlates with pentacoordinated aluminium sites. This can also be detected by the change in binding energy of the 3d electrons of the zirconium.

The acidity of the obtained solid acids was tested by using them as catalysts for the benzolyation of toluene. It was found that a sample with a 50 % zirconium molar percentage possessed the highest surface acidity equalling that of pristine sulfated zirconia despite the reduced mass of zirconia.

Key words: zirconia nanocomposites, catalysts, benzolyation of toluene

• Author to whom correspondence should be addressed (r.frost@qut.edu.au)
P +61 7 313 2407 F: +61 7 3138 1804

INTRODUCTION

Sulfated zirconia was first prepared and explored as a hydrocarbon isomerisation catalyst by Holm and Bailey[1] in 1962. Its unique acid catalytic activity was reported in the literature by Hino *et al.* in 1979, that this catalyst can transform butane into isobutane even at room temperature[2]. Since then, numerous studies using sulfated zirconia as an acid catalyst appeared[3, 4]. It represents a new class of solid strong acid catalysts, and can carry out reactions involving very strong acid sites under mild temperature conditions[5, 6]. Moreover, it possesses distinct advantages in catalyst separation, reactive-system maintenance, compared with traditional liquid catalyst, such as HF and H_2SO_4, which cannot satisfy the stringent environmental restriction on waste disposal[7, 8].

Several zirconium precursors have been reported for the preparation of sulfated zirconia, usually, the catalyst is prepared by first precipitating the hydroxide of zirconium which, after washing and drying, subsequently is treated with a solution of H_2SO_4 and followed by calcination. In the preparation procedures, the pH of precipitation of the hydroxide step[9], and the calcination temperature[10, 11] are found to be particularly important for a high catalytic activity. The optimised calcination temperature is found at 600^oC~ 650^oC to give the highest intrinsic activity[10] corresponding to the formation of theoretical monolayer coverage by the sulfated species. Moreover, the treatment with other sulfurous species, such as $(NH_4)_2SO_4$, SO_2, H_2S, and SO_3 can also promote its catalytic activity[12]. Morterra *et al.*[13] investigated the relationship between the crystal phase of zirconia and their exhibited catalytic activity, and proposed that (i) the sulfation process usually occurs irrespective of sulfating agent; (ii) the zirconia must be tetragonal phase in the final catalyst while the catalyst as monoclinic zirconia is almost inactive as investigated in the isomerisation reaction of n-alkanes; (iii) the catalyst must be activated by calcination at temperatures $T \geq 800K$, at

this temperature, the surface sulfates on tetragonal zirconia are corresponding to a structure, in which the two S=O oscillators almost form an orthogonal angle.

Pristine sulfated zirconia appears as a very promising solid acid catalyst for the replacement of the commercial acid catalyst; however, the catalyst is known to suffer significant deactivation in practical application, possibly due to sulfur leaching or reduction at mild temperatures, active phase transformation from tetragonal phase to monoclinic phase, or the formation of coke on the surface of catalyst[14].

Mounting the sulfate zirconia on an alumina support[11] was proposed to constitute a more stable catalyst capable of resisting deactivation. However, it is hard to attain a high loading of zirconium species on this support because the particle aggregation and sintering during preparations can sufficiently decrease the specific surface area, resulting in negative effect on catalytic activity[15]. Unfortunately, a small loading of zirconia cannot give rise to the highly active tetragonal zirconia[11, 16].

Gao reported[17, 18] that sulfated zirconia promoted by a small amount of alumina by co-precipitation exhibited excellent catalytic activity and also improved stability at the temperature higher than 250^{o}C for n-butane isomarization. The roles of alumina were investigated by several groups[18-20]. The increase in activity for n-butane isomerisation was attributed to a significant increase in the concentration of active sites. Addition of Al_2O_3 also results in the formation of smaller crystallites of ZrO_2 which stabilize the active tetragonal phase of ZrO_2. The presence of smaller crystallite sizes of the tetragonal phase of ZrO_2 after Al_2O_3-promotion affects the total surface area, sulfur content and the number of active sites.

However, the samples prepared by co-precipitation or sol-gel method have an inherent limitation. During the preparation of ZrO_2/Al_2O_3 nanocomposite, as a result of the homogeneous distribution of Zr and Al at atomic level, the addition of only a small fraction of aluminium by these methods will result in a significant elevation of calcination temperature for the phase transformation from the resultant amorphous precipitate to tetragonal ZrO_2 nanocrystallites. For example, as reported in Gao's papers [17, 18], the addition of 15 mol% Al_2O_3 in the synthesis of Al_2O_3-promoted sulfated zirconia resulted in an amorphous material after calcination at 650^{o}C. The crystallizing temperature of this material had to be elevated to 750^{o}C to achieve tetragonal structure of zirconia, given the relatively low activity of the amorphous zirconia solid acid[21]. Nevertheless, such high calcination temperature not only decomposed sulfate species, but also resulted in low surface areas of this material[18]. Moreover, the increase of calcination temperature in such a high temperature region will bring about not only extremely large amount of energy waste but also expensive investment for thermal insulation on an industrial scale.

In our previous investigation[22], tetragonal zirconia nanocrystallites were supported on long bundles of alumina nanofibres forming extremely long ZrO_2/Al_2O_3 composite nanorods with a new core-shell structure when the Zr molar percentage was > 30%. Naturally, the resultant materials are a hierarchically macro-mesoporous zirconia material: the evenly distributed ZrO_2 nanocrystallites result in mesoporous zirconia with large surface areas, while the stacking of such nanorods gives rise to a new kind of macroporous material. The stabilised and highly dispersed tetragonal zirconia nanocrystallites observed on fibrous ZrO_2/Al_2O_3 core shell nanocomposites and the unique property of tetragonal zirconia on catalytic application provide intense incentive to us to develop these nanocomposites into a series of novel catalysts. In this work, these fibrous ZrO_2/Al_2O_3 core-shell nanocomposites

were developed as a series of fibrous solid acid with the Zr molar percentage X=100*Zr/(Al+Zr) from 2 % to 50 % via sulfating procedure, followed by calcining at 650^{o}C.

Benzoylation of toluene with benzoyl chloride is an important strong acid-catalysed reaction for the manufacture of aromatic ketones, which are important intermediates in the fine-chemical and pharmaceutical industries. The catalytic performances of many other solid acids, including zeolite[23], Nafion-H on silica[24], heteropolyacids[25] and some sulfated metal oxide[26] such as SO_4^{2-}/γ-Al_2O_3, SO_4^{2-}/ZrO_2 have been evaluated for this reaction to replace some homogeneous acid catalysts used in industry. On sulfated zirconia, the product of the benzoylation of toluene with benzoyl chloride is a mixture of p-, o- and m-methylbenzophenone (scheme 1). The catalytic performances of fibrous sulfated nanocomposites were tested for this reaction. The structure and physicochemical properties of the catalysts were characterized by means of XRD, IES, SEM equipped with EDX, ^{27}Al MAS NMR and the N_2 adsorption/desorption isotherms.

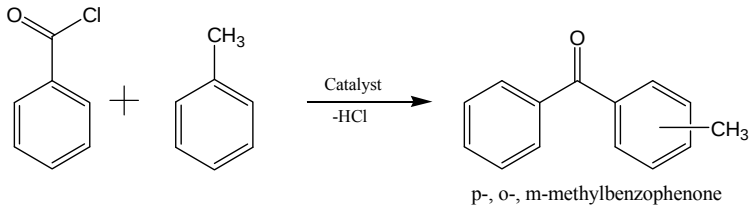

Scheme 1. Benzoylation of toluene with benzoyl chloride

EXPERIMENTAL SECTION

Materials: Boehmite fibres were synthesized by steam-assisted, solid wet-gel method according to literature reports[27]. Butanol was purchased from Ajax Finechem and zirconium (IV) tert-butoxide solution (80 wt. % in 1-butanol) was purchased from Aldrich. All these chemicals are used as received.

Nanocomposite preparation: fibrous $Zr(OH)_x$-boehmite nanocomposites were synthesized by deposition of zirconia species on the boehmite nanofibres. In a typical procedure, 0.39 g boehmite nanofibres was added with 0.20g deioned water which was then dispersed into 20 ml butanol under vigorous stirring. Zirconium (IV) butoxide was dissolved into the resultant mixture solution according to the Zr molar percentage X=100*Zr/(Al+Zr)= 2%, 5%, 10%, 15%, 30%, with stirring for 5 min. The nanocomposite with 50 % of Zr molar percentage was synthesized by the same procedure as mentioned above, except that 0.39g boehmite nanofibres was added with 0.40g deioned water, as the hydrolysis of additional zirconium butoxide consumes more water. Subsequently, the solutions were transferred into autoclaves for hydrothermal reaction at 170^{o}C for 24 hours. After cooling to room temperature, the resulting nanocomposites were separated by centrifugation, and then dried at 80^{o}C for 1 day.

Catalyst preparation: To prepare fibrous sulfated nanocomposites, as-synthesized fibrous $Zr(OH)_x$-boehmite nanocomposites with various Zr molar percentage were precalcined at 300^{o}C for 3 hours and re-dispersed into a 0.5 M H_2SO_4 solution (15 ml/g). After 30 min, the samples were separated by centrifugation and dried at 80^{o}C for 24 h, followed by calcination at 650^{o}C in air for 3 h. These sulfated fibrous nanocomposites are labelled as S-Zr-"m", where m is Zr molar percentage.

For comparison, sulfated zirconia, sulfated alumina and two kinds of commercial zeolites (H-ZSM-5, HY) were chosen as reference catalysts. Sulfated zirconia was prepared according to the procedures in the literatures[17, 28]: Amorphous $Zr(OH)_4$ was prepared by dropwise addition of aqueous ammonia into a zirconyl solution until pH 9. After washing and drying,

146 the sample was immersed in a 0.5 M H_2SO_4 solution for 30 min followed by separation from
147 the liquid phase. Without washing, the sulfated zirconia was dried at 80^oC and calcined at
148 650^oC in air for 3 h. The resulting catalyst was labelled as SZ. Sulfated alumina was prepared
149 by immersing boehmite nanofibres into a 0.5 M H_2SO_4 solution for 30 min followed by
150 separation from the liquid phase. The sample was dried at 80^oC for 24 h, calcined at 650^oC
151 for 3 h and labelled as SA-F.
152
153 ZSM-5 was purchased from Zeolyst international (CBV 2314), USA, and zeolite Y was
154 supplied by FuSheng dyestuff factory, China. All the zeolites were received in the
155 ammonium form, and were transformed into corresponding H-zeolites by calcination at
156 550^oC for 6h. The surface area of commercial H-ZSM-5 was 425 m^2/g and its reported Si/Al
157 ratio was 11.5. The surface area of commercial HY was 648 m^2/g and its reported Si/Al ratio
158 was 3.
159
160 **Characterization:**
161 *Sulfate contents* of all samples were determined by ion chromatography. The instrument is
162 a Dionex RFIC 2100 ion chromatograph with a Dionex AS-18 4mm×100mm analytical
163 column and an AS18 4mm×25mm guard column. An isocratic 33mmol KOH solution was
164 used as eluent. All sulfated powdered sample was suspended in 0.1M NaOH and filtered
165 through a 0.5-μm PTFE filter.
166
167 *XRD patterns* were collected on a PANalytical X'Pert PRO X-ray diffractometer (radius:
168 240.0 mm). Incident X-ray radiation was produced from a line-focused PW3373/10 Cu X-ray
169 tube, operating at 40kV and 40mA, providing a $K\alpha_1$ wavelength of 1.540596 Å. The incident
170 beam passed through a 0.04 rad Soller slit, a ½ divergence slit, a 15mm fixed mask, and a 1°

171 fixed antiscatter slit. After interaction with the sample, the diffracted beam was detected by
172 an X'Celerator RTMS detector, which was set in scanning mode, with an active length of
173 2.022mm. Diffraction patterns for the samples were collected over a rage of 3~ 75^{o} 2θ.
174
175 *XPS data* was obtained on a Kratos Axis ULTRA X-ray photoelectron spectrometer. The
176 incident radiation was monochromatic Al X-rays (1486.6 eV) at 150W (15kV, 15ma). The C
177 1s peak at 284.5 eV was used as a reference for the calibration of binding energy scale.
178
179 *Surface Area Analysis* based on N_2 adsorption/desorption techniques were performed on a
180 Micrometrics Tristar 3000 automated gas adsorption analyser. Samples were pretreated at
181 200^{o}C under the flow of N_2 for a minimum of 5 h on a Micrometrics Flowprep 060 degasser.
182
183 *SEM micrographs* were obtained on a FEI QUANTA 200 scanning electron microscope
184 operating at 30kV accelerating voltage with a 2.5 spot size. The samples were dried at room
185 temperature and coated with gold under vacuum conditions in an argon atmosphere ionization
186 chamber to increase surface conductivity.
187
188 *FT-IR emission spectroscopy* was carried out on a Nicolet spectrometer modified by
189 replacing the IR source with an emission cell. The description of the cell and principles of the
190 emission experiment have been published elsewhere[29].
191
192 *Solid-state ^{27}Al MAS NMR spectra* were obtained from Varian Driver spectrometer
193 operating at a resonance frequency of 104.26 Hz with a recycling time of 0.5 s. The spinning
194 frequency was no lower than 7 KHz.
195

Transmission electron microscopy was carried out on a Phillips Tecnai F20 TEM. The instrument was equipped with a Field Emission Gun source operating at a High Tension of 200kV.

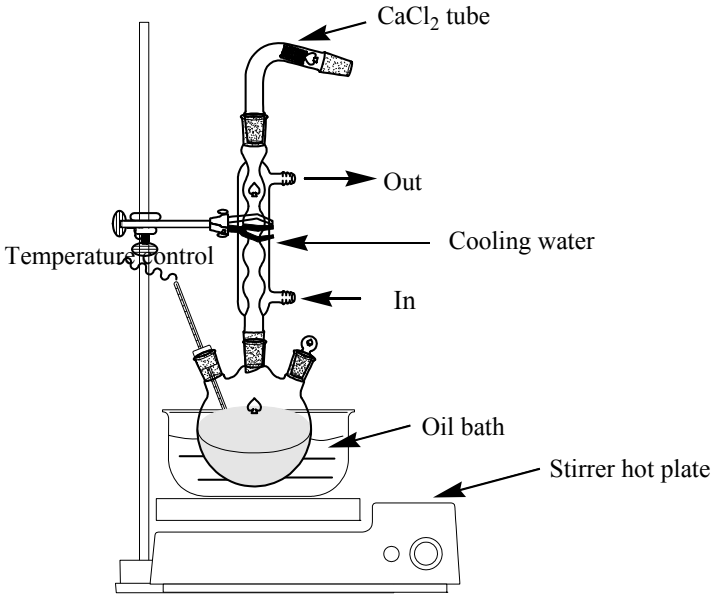

Scheme 2. Schematic diagram of catalytic reactor for Benzoylation of toluene with benzoyl chloride

Benzoylation reaction:

Benzoylation of toluene with benzoyl chloride was used to investigate the catalytic activity of a series of fibrous nanocomposite superacids. The reaction was carried out in a round-bottom flask equipped with a reflux condenser connecting with a $CaCl_2$ tube which is used to keep the reaction system free of moisture (Scheme 2). Before reaction, all catalysts were freshly activated at 500 ^oC for 2.5 hours and cooled down to ambient temperature in an argon atmosphere in order to remove the adsorbed water molecules on the surfaces of the catalysts. 0.4 ml benzoyl chloride, 8 ml toluene and 0.2 g catalysts were charged into the reactor which was heated to reflux (*ca*. 110^oC) in an oil bath under magnetic stir. Samples were collected at some specific intervals and immediately analysed by gas chromatography. Quantitative results were obtained by comparing the results with the calibration from synthetic mixtures.

Since toluene was in excess, the yields of methylbenzophenone were based on the benzoyl chloride added into the reaction.

RESULTS

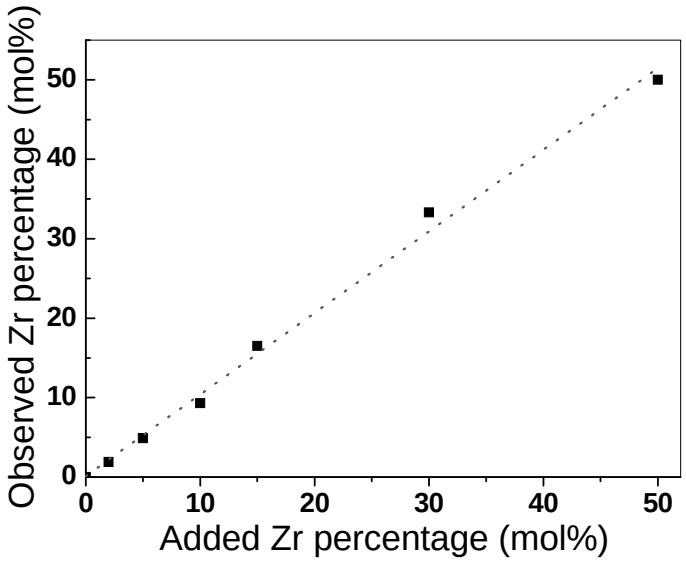

Figure 1. Observed Zr percentage in samples as a function of nominal Zr percentage (measured by EDX)

The overall compositions of all the fibrous nanocomposites prepared with various Zr/Al molar ratios were examined by EDX equipped on SEM. The area selected was approximately 0.04 mm^2 at each run, and at least five different spots were selected for each sample to get an average value of the composition. As shown in Figure 1, the observed Zr percentage is equal to the nominal molar ratio, indicating all of zirconium precursors were precipitated from the mixture solution and deposited on the boehmite nanofibres.

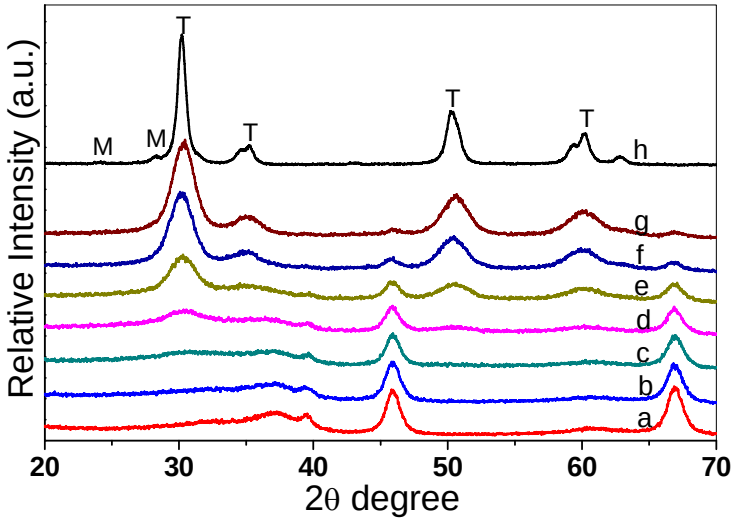

Figure 2. XRD patterns for the sulfated fibrous ZrO_2/Al_2O_3 nanocomposites, alumina nanofibres and zirconia obtained by calcination at 650°C for 3 h. (a) sulfated alumina nanofibres (b) S-Zr-2, (c) S-Zr-5, (d) S-Zr-10, (e) S-Zr-15, (f) S-Zr-30, (g) S-Zr-50 and (h) sulfated zirconia. M and T represent monoclinic phase and tetragonal phase, respectively. The patterns in (H) underwent a 0.6-fold Y-scale reduction

The XRD patterns of the sulfated fibrous ZrO_2/Al_2O_3 nanocomposites obtained by calcination at 650°C for 3 h are shown in Figure 2. The phase of sulfated alumina nanofibres illustrates the γ-Al_2O_3 structure. The peaks at 45.8 and 66.8 °2θ correspond to the diffractions from (400) and (440) planes of γ-Al_2O_3. For pristine sulfated zirconia, a small portion of the monoclinic phase presents besides the tetragonal phase. The peaks at 30.2, 35.3, 50.3 and 60.1 °2θ are attributed to the diffractions from (101), (110), (112) and (211) planes of tetragonal zirconia while the peaks at 24.5, 28.2 °2θ are the diffractions from (-110) and (-111) planes of monoclinic zirconia. In contrast, for these sulfated fibrous nanocomposites, as Zr molar percentage is higher than 10 %, the nanocrystallites of tetragonal zirconia can be detected by the appearance of a broadened peak at ca. 30°. The intensity of this diffraction, as well as others for tetragonal zirconia, increases with the increase of zirconia percentage, but no peak corresponding to monoclinic zirconia is observed in the patterns for all these nanocomposites. Meanwhile, the diffraction peaks for γ-Al_2O_3 gradually decrease and

249 become undetectable at 50 mol% of Zr due to the reduction of relative concentration of the γ-
250 Al_2O_3 and its inherently poor intensity.
251
252 The primary crystallite sizes of the tetragonal zirconia in these samples (including the
253 pristine sulfated zirconium and fibrous sulfated ZrO_2/Al_2O_3 nanocomposites) are calculated
254 by the Scherrer equation and listed in Table 1. It can be observed that an increase of Zr molar
255 percentage from 10 % to 50 % resulted in increased main crystallite sizes from 2.1 nm to 4.5
256 nm in (101) direction, which are much smaller than that of the pristine sulfated zirconium at
257 12 nm. As shown in our previous investigation[22], the alumina nanofibres can retard the
258 crystallite size growth of zirconia and therefore retard the transformation of zirconia from
259 metastable tetragonal phase to the monoclinic phase because metastable tetragonal zirconia is
260 stable in small crystal size.
261

Table 1. Crystallite dimension in (101) direction for sulfated tetragonal zirconium and that deposited on alumina nanofibres with various zirconia content (The data were derived from X-ray diffraction patterns)

Sample name	Peak position (2θ)	FWHM (2θ)	Crystallite dimensions(nm)
Sulfated zirconium	30.14	0.684	12.0
S-Zr-50	30.28	1.832	4.5
S-Zr-30	30.12	2.086	3.9
S-Zr-15	30.34	3.057	2.7
S-Zr-10	30.38	4.000	2.1

Figure 3 shows the ^{27}Al MAS NMR spectra of the sulfated fibrous nanocomposites. Although it is possible that some spectral components cannot be distinguished due to peak broadening, some species can be clearly identified via fitting procedures, as shown in Figure 4. The intense signal at *ca*. 5 ppm corresponds to octahedral aluminium Al_{octa} sites (AlO_6), while the relatively weak resonances at around 67 ppm indicates the presence of tetrahedral aluminium Al_{tetra} sites (AlO_4)[30]. These two resonances correspond to the two coordination states of Al in γ-Al_2O_3 crystal structure[31, 32], which complements the XRD results of these nanocomposites. The alumina phase in S-Zr-50 could be confidently identified as γ-Al_2O_3. For all the samples, the resonance peaks corresponding to the AlO_6 are remarkably asymmetric, and a tail in spectra from 0 to -25 ppm can be observed. The tail could be due to the presence of new Al octahedral sites, namely $Al_{octa\text{-}O\text{-}S}$ or $Al_{octa\text{-}O\text{-}Zr}$, where S or Zr is located in the second coordination shell of aluminium[33]. In addition, with the increase in the Zr/Al molar ratio, a resonance between two main peaks centred at about 37 ppm becomes more pronounced. This component has been assigned to pentacoordinated aluminium Al_{penta} sites (AlO_5)[34].

281 It should be noted that in this work, γ-Al_2O_3 is prepared via the phase transformation of
282 boehmite phase which only contains octahedral aluminium Al_{octa} sites (AlO_6). Both of AlO_4
283 and AlO_5 sites are created by the dehydration and dehydroxylaton of AlO_6 at elevated
284 temperature. In Table 2 the relative percentages of the AlO_4, AlO_5 and AlO_6 are listed for the
285 sample with increasing Zr molar percentages. It shows that the AlO_5 sites increase at the
286 expense of both AlO_6 and AlO_4 sites, and the AlO_6 site decreased more rapidly than the AlO_4
287 site. The enhancement of AlO_5 sites with the increase in Zr molar percentages suggests that
288 the penta-coordinated aluminium site is correlated to the surface interaction between zirconia
289 and alumina. Nevertheless, the percentage of AlO_5 sites was not directly affected by the Zr
290 content. For the sample S-Zr-10, the percentage of AlO_5 sites is slightly lower than that for
291 the samples S-Zr-2 and S-Zr-5. Presumably, this is because at 10 mol% Zr, zirconia species
292 transfer into tetragonal nanocrystallites and the Al-O-Zr sites are reduced due to the
293 aggregation of zirconia species. Therefore, it is possible that when zirconia species is in
294 highly dispersed state (S-Zr-2, S-Zr-5), the samples possess more AlO_5 sites.

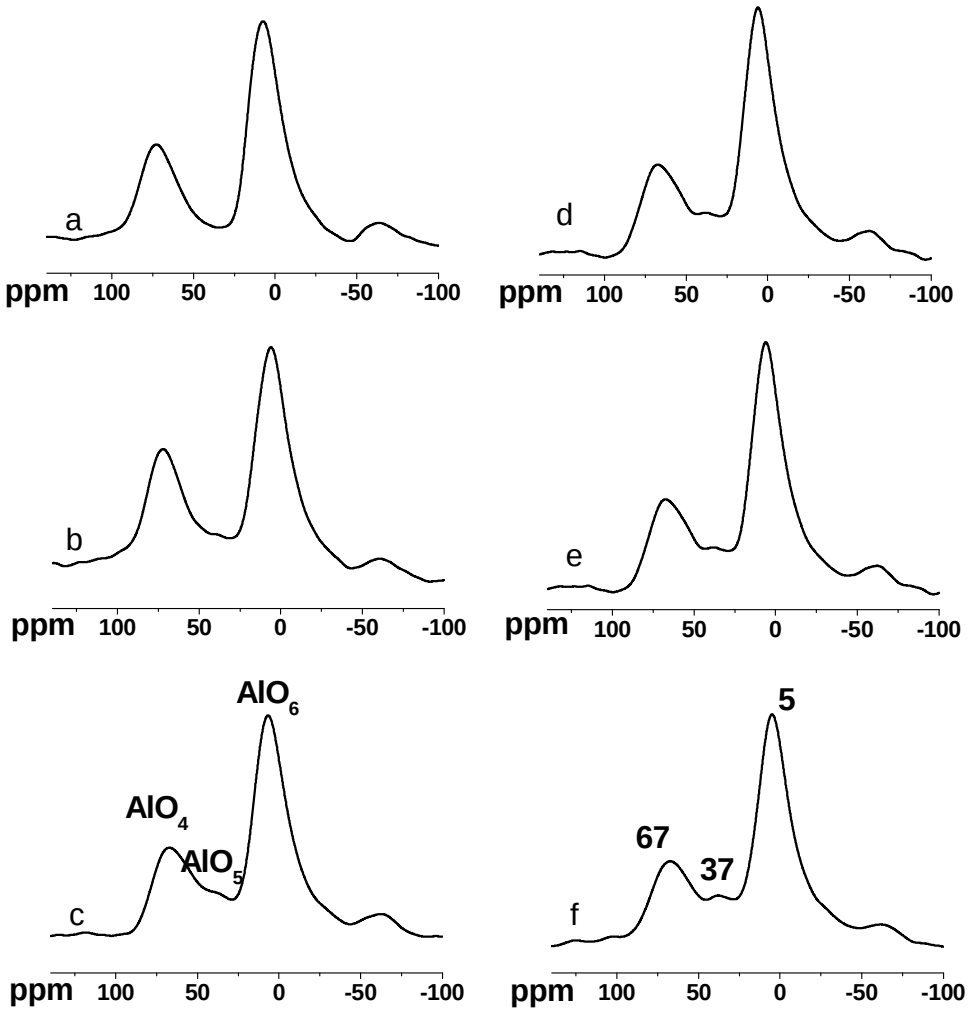

295
296 **Figure 3.** ^{27}Al MAS NMR spectra of sulfated pristine alumina nanofibres and fibrous
297 ZrO_2/Al_2O_3 nanocomposites obtained by calcination at 650^{o}C: (a) SA-F; (b) S-Zr-2; (c) S-Zr-
298 5; (d) S-Zr-10; (e) S-Zr-15; (f) S-Zr-30

299

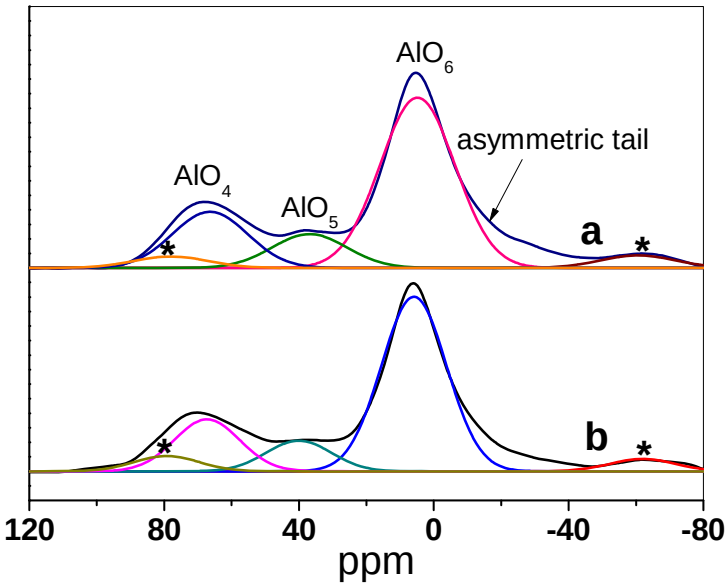

Figure 4. Separated components of (a) S-Zr-30; and (b) S-Zr-50 obtained by spectrum fitting procedure. *quadrupolar sideband

Table 2. The relative percentages of the AlO_4, AlO_5 and AlO_6 species for the nanocomposites with various Zr molar percentages (obtained by spectrum simulation procedure)

Sample name	AlO_6	AlO_5	AlO_4
SA-F	74.8%	0	25.2%
S-Zr-2	65.9%	6.7%	27.4%
S-Zr-5	66.1%	10.5%	23.4%
S-Zr-10	68.3%	7.6%	24.1%
S-Zr-15	67.1%	11.8%	21.2%
S-Zr-30	63.2%	13.8%	23.0%
S-Zr-50	62.1%	14.6%	23.3%

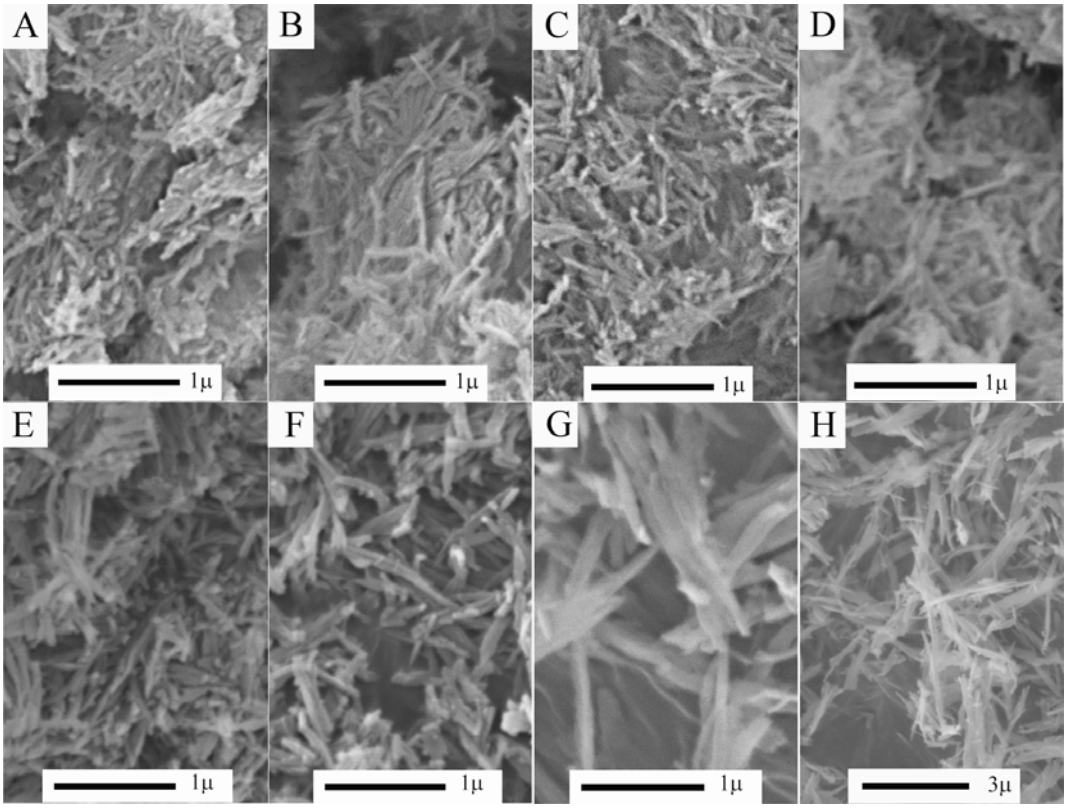

Figure 5. SEM images of sulfated pristine alumina nanofibres and fibrous ZrO_2/Al_2O_3 nanocomposites obtained by calcination at 650°C: A) SA-F; B) S-Zr-2; C) S-Zr-5; D) S-Zr-10; E) S-Zr-15; F) S-Zr-30; G) S-Zr-50; H) S-Zr-50 at a larger scale

Particle morphology is investigated by SEM as shown in Figure 5. The image for sulfated pristine alumina nanofibres shows many entangled worm-like particles. The fibrous morphology for this kind of material generates large inter-particle voids, which are referred to as porosity of this material. Importantly, after the sulfating procedure and calcination, the materials also retain their fibrous morphology which can be clearly observed from their SEM images. This structural stability is probably a result of the starting material, boehmite nanofibres, being relatively stable in sulfuric acid solution. This nanostructure is constituted by a singular or small bundle of nanofibres as a hard template and is further fixed by the zirconia shell. This zirconia shell is essential to maintain the integrity of the nanocomposite fibres. Therefore, short and thin nanofibres formed at low zirconia coverage and relatively large nanorods are observed when Zr percentage is higher than 15 %. The porosity and pore

volumes of these nanocomposites are dependent on the diameter and length of their constituted nanorods, which increase with the increase of Zr content, consequently, the macroporous frameworks resulting from specific morphology of fibrous nanomaterials are also gradually extended.

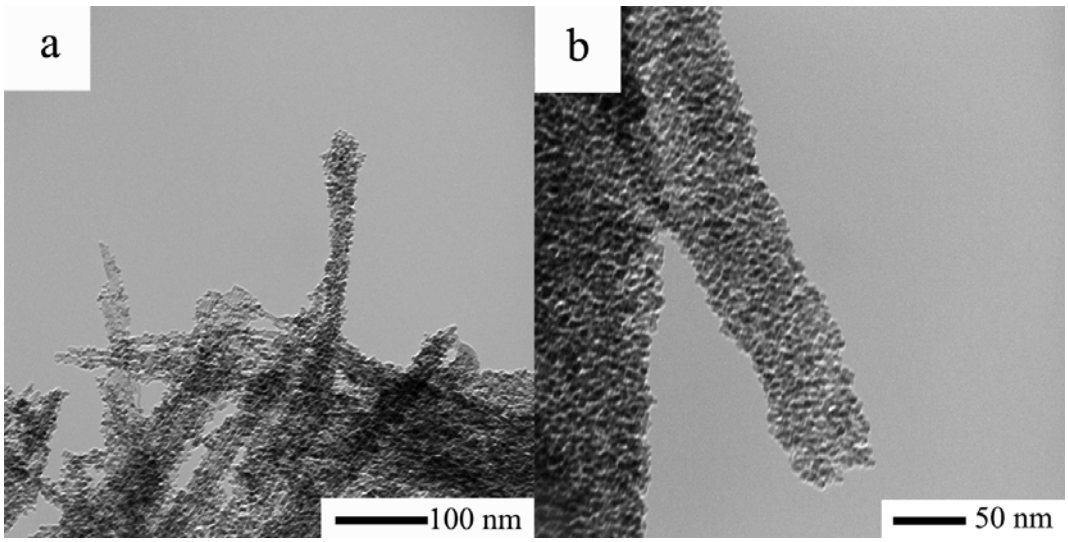

Figure 6. TEM image for a) S-Zr-30 and b) S-Zr-50

The transmission electron microscopy (TEM) images of S-Zr-30 and S-Zr-50 are illustrated in Figure 6. Such solid acid nanocomposites exhibit a novel fibrous morphology where sulfated tetragonal zirconia shows irregular squares covering the alumina bundles. It can be observed that even at 30 mol % Zr content the sulfated tetragonal zirconia is still insufficient to cover the entire outer surface of alumina bundles while only at 50 mol % of Zr the bare alumina bundles are fully covered, indicating the outer surface of alumina bundles can bear an extremely large Zr content.

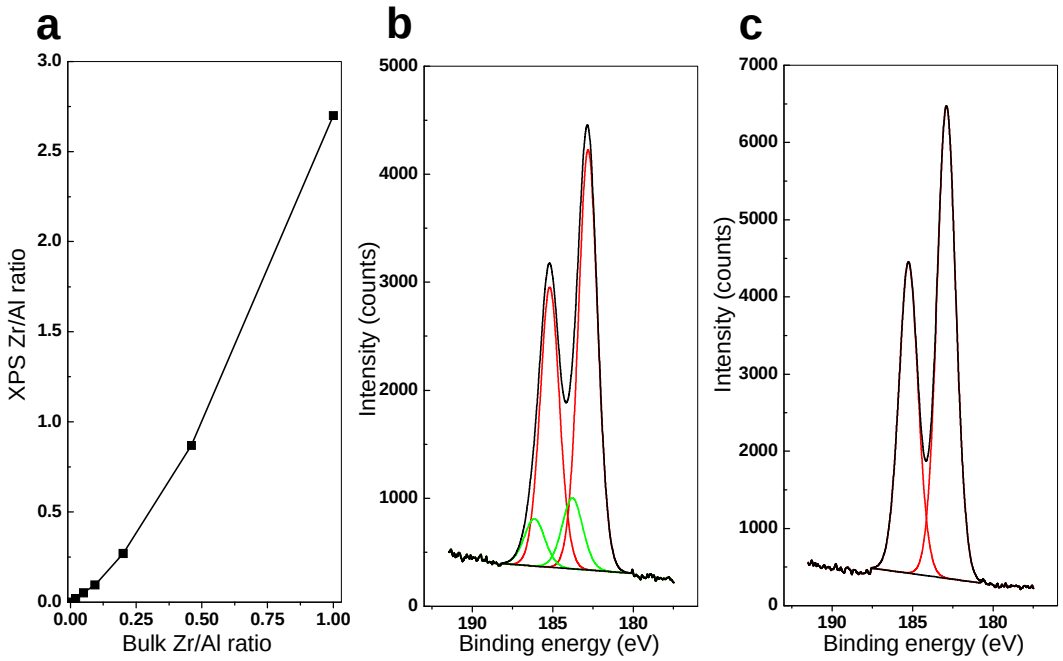

Figure 7. XPS results a) XPS Zr/Al molar ratio as a function of bulk Zr/Al molar ratio, b) Zr 3d XPS spectra of S-Zr-30 and c) Zr 3d XPS spectra of S-Zr-50

XPS analysis of pristine sulfated zirconia and all ZrO_2/Al_2O_3 nanocomposites was investigated and all samples were measured after crushing. Figure 7a shows the Zr/Al XPS surface atomic ratios as a function of the corresponding overall ratios measured by EDX. When Zr molar percentage is equal to or less than 15%, the XPS ratios are very close to the bulk ratios. Above this value, the XPS surface ratios gradually become much higher than bulk ratio. Especially for the S-Zr-50, of which the bulk Zr/Al molar ratio is 1:1, the XPS surface ratio is close to 3:1, indicating the Zr species is concentrated on the outer surface of alumina nanobundles.

In addition, for S-Zr-50, the $Zr3d_{5/2}$ photopeak centred at binding energy of 182.9 eV (Figure 7c), and only one chemical environment of Zr could be detected. This is the same with the result for pristine sulfated zirconia reported in the literature[35]. The interaction between the ZrO_2 species and Al_2O_3 support can only be detected when Zr molar percentage

355 is lower than 30 %, the Zr3d photopeaks can be decomposed into two components (Figure
356 7b). The binding energy of $Zr3d_{5/2}$ for one component is the same as pristine sulfated zirconia,
357 and the other exhibits a displacement for the bonding energies of $Zr3d_{5/2}$ of 0.9 eV, to about
358 183.8eV. This displacement has been associated with the formation of Zr-O-Al-type
359 bonds[36]. The ratio of the latter component increases with decreasing of zirconium content,
360 which is summarised in Table 3.

361 **Table 3.** The binding energies of $Zr3d_{5/2}$ photopeak corresponding to two kinds of Zr species
362 and their relative ratios in XPS spectra

Sample	Zr $3d_{5/2}$			
	ZrO_2	Percentage	Zr-O-Al	Percentate
S-Zr-50	182.9	100 %	———[a]	———[a]
S-Zr-30	182.9	85 %	183.8	15 %
S-Zr-15	182.9	63 %	183.8	37 %
S-Zr-10	182.9	63 %	183.8	37 %
S-Zr-5	183.0	60 %	183.8	40 %
S-Zr-2	183.0	52 %	183.8	48 %

363 [a] Cannot be detected by XPS

364

365

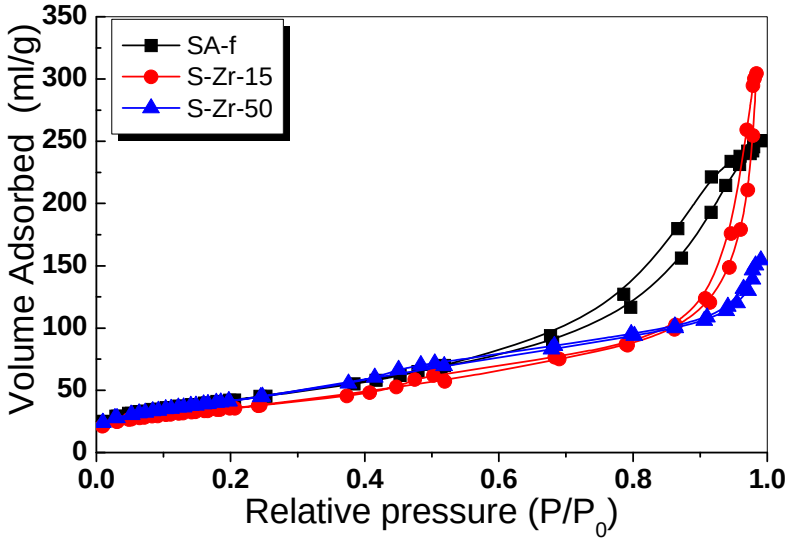

Figure 8. Nitrogen adsorption and desorption isotherms for some representative samples with various Zr molar percentages

The BET surface areas and pore structures of these catalysts are determined by nitrogen adsorption-desorption isotherms. Figure 8 shows those for representative samples to illustrate the textural changes with the increase of the Zr molar percentage. Accordingly, all the isotherms show a type IV characteristic feature of isotherm, which indicates that the samples examined are full of mesopores[37]. For S-Zr-50, the isotherms at high P/P_0 show a type II characteristic feature, which is often obtained in a macroporous material. The hysteresis of the three samples is quite different. The hysteresis loop of the sulfated alumina nanofibre falls within H3 and H4 categories, which, according to Sing's study[38], should be a result of slit-like pores constructed by plate-like particles. However this sample has the morphology of nanofibres. Therefore, the arrangement of nanofibres must also give rise to this kind of loop. The hysteresis for S-Zr-15 exhibits a loop with two steps: at high P/P_0 from 0.8 ~1.0, the hysteresis loop is close to H3, which show a higher slope ratio indicating wide slit-like pores; another step of hysteresis loops remains nearly horizontal over a wide range of P/P_0 from about 0.42 ~ 0.8, which is similar to the type H2 loop, associated with bottle ink pore or pore networks[39]. The former part is produced by the stacking of fibrous particles and the latter part is generated by the coating of zirconia nanocrystals and this is also observed for the

sample S-Zr-50. For S-Zr-50, the adsorption branch and desorption branch overlapped at P/P_0 from 0.8~1.0, the isotherm become a combination of type II and IV adsorption, indicating the nanocomposite containing both mesopores and macropores[38].

The pore size distributions of as-synthesized nanocomposites are estimated from the adsorption branch of isotherm to avoid ambiguities arising from tensile strength effects[40]. Sample SA-F has a wide pore size distribution from 1 nm to 100 nm, which is the characteristic feature of pores arising from the intercrystallites voids constructed by nanofibres. All nanocomposites show two distributions from 1-8 nm and above 10 nm, respectively. The former distribution is attributed to the pores formed by incorporation of zirconia species and the latter one is assigned to those formed due to their fibrous morphology. It can be observed that the distribution from 1-8 nm gradually increases, while the latter distribution decreases with the increase of Zr content. At 50 mol% Zr, pore size is mainly distributed in the range of 2-8 nm, the inter-particle voids resulting from fibrous nanostructure almost disappear. This phenomenon was also observed in our previous work[22] and is due to the increase of Zr mol% enhances the structural integrity (length and diameter increase) of resultant nanorods and the porous frameworks constructed from these fibrous nanocomposites gradually expand, leading to the most of macropores exceeding the measurable range for N_2 physisorption.

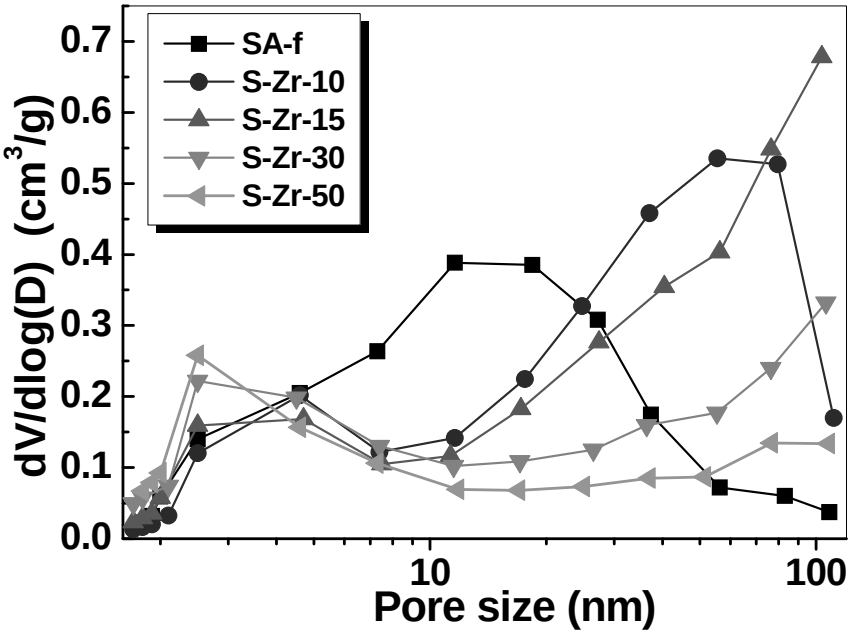

406

407 **Figure 9.** Pore size distributions for samples with various Zr content

408

409

410 The main textural parameters for sulfated samples after calcination at 650°C and original
411 boehmite nanofibres are listed in Table 4. Many literatures confirm that loading even small
412 amount of zirconia on alumina would result in a decrease in surface area, most prominently
413 when zirconia crystal phase begins to appear, the surface area would dramatically be
414 decreased below 100 m^2/g[11, 16, 41]. However, interestingly in this work, samples with
415 differing zirconia loading on alumina nanofibres actually maintain a relatively constant high
416 specific surface area. The specific surface areas for all as-synthesized nanocomposites vary
417 from 125 to 154 m^2g^{-1}. In contrast, the pristine sulfated zirconia has a surface area at about 88
418 m^2g^{-1}, similar to that reported in literature[20]. The sulfated alumina nanofibres exhibit a
419 similar surface area, average pore size and pore volume comparing with original boehmite
420 nanofibres.

421 **Table 4.** Powder properties of the sulfated fibrous ZrO_2/Al_2O_3 nanocomposites with various
422 Zr molar percentage and sulfated alumina nanofibres obtained by calcination at 650°C

Sample	BET surface	Average pore	Pore volume

	area($m^2g^{-1)}$	size (nm)	(cm^3/g)
Boehmite nanofibres	158	13.32	0.525
SA-F	152	10.16	0.387
S-Zr-2	138	16.42	0.565
S-Zr-5	131	16.47	0.540
S-Zr-10	125	15.74	0.491
S-Zr-15	128	14.67	0.471
S-Zr-30	154	8.26	0.318
S-Zr-50	153	6.25	0.239
SZ	88	7.69	0.169

423

424 The sulfated zirconia is an important solid acid catalyst. However, its acid strength is still
425 in debate. At the very beginning, sulfated zirconia was claimed to be a superacid which was
426 defined as a material with acidity stronger than 100% H_2SO_4[42]. The acid strength of
427 sufated zirconia was measured by the change in color of a Hammett indicator at $pK_a \leq -14.52$,
428 was estimated to be $H_0 \leq -16.04$. Based on this, the acidity was considered to be 10000 times
429 stronger than 100% perchloric or sulfuric acid[2]. However, When Umansky *et al.*[43] used
430 the same Hammett indicator to measure the acidity of sulphated zirconia and recorded the
431 color change by UV spectroscopy to minimize the experimental subjectivity, he reported that
432 the acidity of sulfated zirconia was only equivalent to 100% H_2SO_4. Indeed, the use of
433 Hammett indicators is also considered to be unreliable for the accurate measurement of solid
434 acidity[44], because it was hard to achieve the equilibrium measurement using these
435 indicators[45].

436

437 The superacidic protons of sulfated zirconia has been detected by 1H NMR and Raman
438 spectroscopic studies[46], and was considered to be significantly stronger than H-ZSM-5.
439 Corma *et al*.[47] also reported the detection of superacid sites using temperature-programmed
440 desorption of NH_3. However, the validity of some traditional techniques, such as
441 temperature-programmed desorption[48, 49] and IR study of pyridine adsorption[50] have
442 been questioned for the determination of the acidity of sulfated zirconia, and was believed to
443 inevitably misestimate the acidity of this kind of material. In contrast, numerous investigators
444 have claimed that the acid strength of sulfated zirconia is similar to H-ZSM-5 and is only a
445 strong acid, this was indicated by some advanced characterisation technologies, including ^{1}H,
446 ^{13}C NMR spectroscopy[51], microcalorimetry[52-54], infrared shifts of OH groups[55-57].
447
448 The measurement of acid strength of a solid acid is much more complex than determining
449 that of a liquid acid. The solid acids are heterogeneous and the accessibility of acid sites
450 makes the determination of acid strength of solid acids difficult[58]. Accurate evaluating of
451 acid strength of solid acid is still challenging at this time[59, 60]. Therefore, it is not
452 surprising that different characterisation techniques will lead to discrepancies in results.
453 Under these circumstances, the relative acid strength is measured in this work.
454
455 Figure 10 shows the Fourier transform infrared emission spectroscopy (IES) of sulfated
456 ZrO_2/Al_2O_3 nanocomposite (S-Zr-50) from 50^{o}C to 350^{o}C. According to the literature, the
457 surface sulfur complexes formed by the interaction of metal oxides with sulfate ions, after
458 evacuation at above 350^{o}C, exhibit a strong band at 1382~1391cm^{-1} in mid-infrared
459 spectroscopy which is assigned to S=O stretching vibration[17, 61]. This band has a strong
460 tendency to reduce its wavenumber with the adsorption of basic molecules such as H_2O. This
461 wavenumber shift, corresponding to a decrease in the bond order of S=O covalent bond and

462 an increase in the partial charge on oxygen atom[61], is associated with the acid strength of
463 the catalyst, where larger wavenumber shifts correspond to higher acidity. Measuring the
464 wavenumber shift of S=O by infrared spectra is regarded as a recommended method to detect
465 the relative acid strength of the sulfated oxide catalysts[17, 18].
466
467 Moreover, IES can measure the vibration wavenumbers of the samples *in-situ* at elevated
468 temperature, which avoids the re-adsorption of water molecules on the surfaces of materials,
469 just after dehydroxylation, due to exposure to air in either the quenching or infrared
470 measurement step. As shown in Figure 10, the IES of S-Zr-50 at 50 ^{o}C shows S=O bonds
471 vibration centred at 1350 cm^{-1} and a broad band near 1630 cm^{-1} corresponding to the bending
472 vibrations of the surface water and hydroxyl group, which can be observed at the same time.
473 As the heating temperature increasing, the S=O bonds vibration become stronger and shift
474 from 1350 at 50 ^{o}C to 1391 cm^{-1} at 350 ^{o}C, and at this temperature, the hydroxyl group
475 bending vibrations almost disappeared. Notably, in this work, the band position
476 corresponding to the stretching vibration of S=O bond of sulfated zirconia obtained at 350 ^{o}C
477 agrees well with that of the same sample previously described in Gao's work[18] which was
478 detected by infrared absorption spectroscopy at room temperature after evacuating at 350^{o}C,
479 indicating that this S=O wavenumber shift is due to the dehydrolysis of samples rather than
480 the change of measuring temperature.

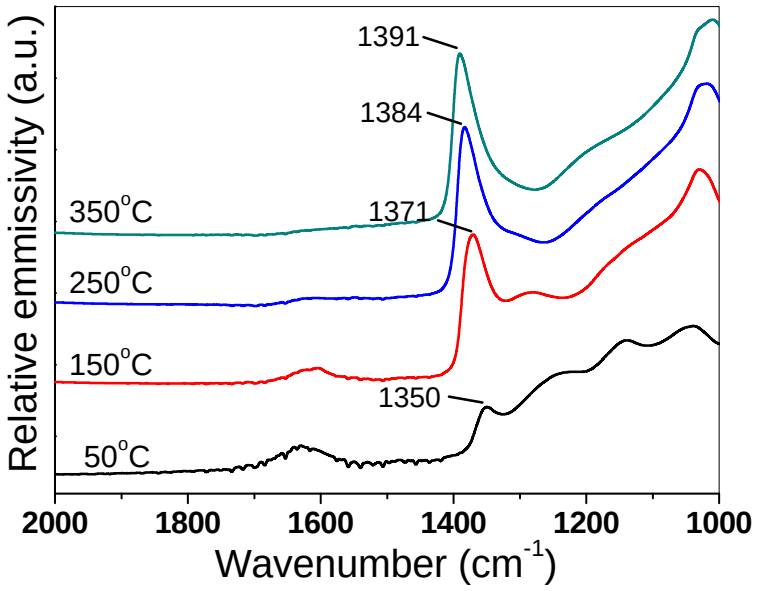

Figure 10. Infrared emission spectra of S-Zr-50 in the region 2000~ 1000 cm^{-1} from 50°C to 350°C at 100°C intervals

Obviously, the spectra obtained at 50°C represent the situation that the water is absorbed on the sulfated catalyst, and those obtained at 350°C correspond to the samples previously evacuated at 350°C. According to a literature[17], the relative acid strength of sulfated fibrous ZrO_2/Al_2O_3 nanocomposites with different Zr molar percentage can be determined by measuring the S=O shifts from 50°C to 350°C based on the IES results. The S=O stretching wavenumber, the bond order and partial charge on oxygen atom calculated according to formulations in the literature[61] for the series of sulfated ZrO_2/Al_2O_3 nanocomposites with different Zr molar percentage are presented in Table 5.

Although there is a slight deviation between this work and Gao's work due to the use of different experimental technology, it can be clearly observed that the S=O shifts of this series of samples increased with the increase of zirconia loading from 0 to 50%. On the other hand, when Zr content is 50%, the shift of S=O stretching is almost identical to that of the sulfated zirconia, indicating similar relative acid strength between S-Zr-50 and SZ. The relative acid

499 strengths are in the order of SA-F <S-Zr-2 <S-Zr-5 <S-Zr-10 <S-Zr-15 <S-Zr-30 < S-Zr-50

500 ≈SZ.

501 **Table 5.** Effect of Water Adsorption on S=O including Stretching Frequency, Bond Order
502 and Partial Charge on Oxygen

Sample	S=O wavenumber(cm^{-1})			Bond order		Partial charge on oxygen	
	B[a]	A[b]	Shift	B	A	B	A
SA-F	1378	1351	27	1.84	1.80	-0.16	-0.20
S-Zr-2	1380	1350	30	1.85	1.80	-0.15	-0.20
S-Zr-5	1382	1350	32	1.85	1.80	-0.15	-0.20
S-Zr-10	1384	1350	34	1.86	1.80	-0.14	-0.20
S-Zr-15	1387	1350	37	1.86	1.80	-0.14	-0.20
S-Zr-30	1389	1350	39	1.86	1.80	-0.14	-0.20
S-Zr-50	1391	1350	41	1.86	1.80	-0.14	-0.20
SZ	1391	1350	41	1.86	1.80	-0.14	-0.20
SZ[c]	1392	1352	40	1.87	1.80	-0.13	-0.20

503 [a] Before water adsorption; measured at 350°C

504 [b] After water adsorption; measured at 50°C

505 [c] Date from Gao's work in Ref 18.

506

507 The sulfate contents in all samples are determined by ion chromatography. Based on the
508 surface area of each material, the densities of SO_4^{2-} groups could also be estimated, ranging
509 from 1.8 to 3.4 per nm^2. Given that the thermochemical radius of SO_4^{2-} is 2.30 Å[62], the
510 value of the density of SO_4^{2-} groups may correspond to a monolayer dispersion of isolated
511 SO_4^{2-}, assuming that the dispersion on the surface of all nanocomposites are homogeneous.
512 However, the density of SO_4^{2-} groups for nanocomposite samples is obviously higher that of
513 pristine sulfate samples (pristine ZrO_2 and Al_2O_3). In this work, it achieves maximum when

514 Zr molar percentage is 10%. Therefore, it can be inferred that the interface of alumina and
515 zirconia nanocrystallites could graft much more sulfate ion than a pristine metal oxide surface.

516 **Table 6.** Surface area and sulfate content of various samples

Samples	Surface area(m^2/g)	SO_4 content		
		(wt%)	(μmol/g)	(groups/nm^2)
SAF	152	4.57%	452	1.8
S-Zr-2	138	4.34%	568	2.5
S-Zr-5	131	5.15%	536	2.5
S-Zr-10	125	6.70%	698	3.4
S-Zr-15	128	6.36%	663	3.1
S-Zr-30	154	5.86%	610	2.4
S-Zr-50	153	4.44%	463	1.8
SZ	88	2.52%	263	1.8

517

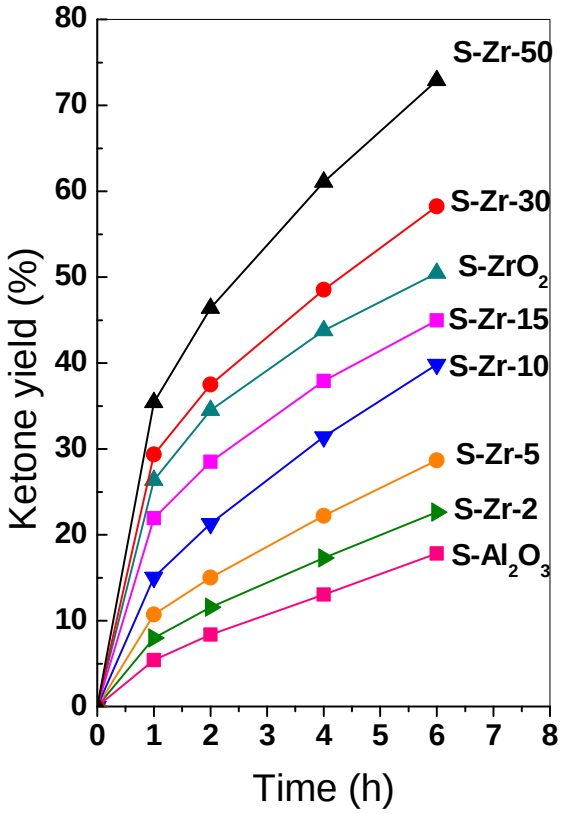

Figure 11. Benzoylation of toluene at 110°C

Benzoylation of toluene with benzoyl chloride is used to investigate the liquid acid-catalytic activity of as-synthesized fibrous solid catalysts. For all these sulfated nanocomposite catalysts, the products of the benzoylation reaction of toluene are a mixture of *p*-, *o*- and *m*-methylbenzophenone, respectively, which is 67~69% of *p*-methylbenzophenone, 27~ 29% of *o*-methylbenzophenone, and 3~ 4% of *m*-methylbenzophenone.

The catalytic activities of samples with different zirconia content are illustrated in Figure 11. The temperature of reaction system is stabilised at reflux. From Figure 11, it can be observed that when Zr content is up to 5%, the ketone yield is less than 25% for 6 hours, but it is about 10 % higher than that of the sulfated pristine alumina nanofibres. As Zr content increases to 10%, the catalytic activity dramatically rises. The activity of the composite exceeds that of sulfated pristine zirconia at or above 30% Zr molar percentage. The overall

tendency is that the catalytic activities increase with the increase in zirconia amount from 2% to 50%.

The ketone yield for H-Y is only 1.3% in 6 hours, and it is only 2.6% for H-ZSM-5. However, the selectivity of products for zeolite catalysts are different from these sulfated nanocomposites catalysts. For zeolite HY, the selectivity for *p*-product is 78.3% and 21.6% for *o*-product. No *m*-product is observed because of the low productivity. For zeolite H-ZSM-5, the selectivity for *p*-product is 83.8%, 8.4% for *m*-product and 7.8% for *o*-product. Their different selectivity strongly indicates their differences in diffusivity. H-ZSM-5 possesses higher selectivity for *p*-methylbenzophenone attributed to its smaller pore size (5.5×5.9Å) comparing with that of zeolite Y (7.4Å)[63].

The relative acidities of sulfated catalysts are determined by IES in this work. It is believed that benzoylation reaction only proceeds on the very strong acid sites which are strong enough for the generation of the reaction intermediate, $PhCO^+$ cation[64]. Since the strong acid sites for all these nanocomposites catalyst are generated by the grafting of sulfate ions, their amount can be evaluated from their sulfate contents, which are almost constant with the increase of Zr mol% due to the similar surface areas of these catalysts. Combined with their relative acid strength of these catalysts, the catalytic performances of all nanocomposites exhibit that the stronger the relative acidity is, the higher the catalytic activity is. The catalytic activity dramatically rises at 10 Zr mol%. Taking the XRD results into account, tetragonal zirconia starts to form until the Zr mol% is above 10%, and with the increase of the Zr mol% the amount of tetragonal zirconia in the sample increases. This result, which coincides with the activities of samples, suggests the increase of tetragonal zirconia might relate with the enhancement of surface acidity of the catalyst.

The acid strength of H-ZSM-5 is stronger than that of HY, and its catalytic activity is also higher than that of HY in our experiment. Despite their poor catalytic activities, the correlation that stronger acid sites lead to higher catalytic activity is also complied by zeolite catalysts. It cannot be excluded that the low catalytic activities of H-ZSM-5 and HY in this reaction are possibly due to the lower accessibility of their acid sites in the narrow channels of zeolites. However, it should be mentioned that the solid acid possesses both Brønsted acid site (protonic sites) and Lewis acid sites (an electron-pair acceptor). The Brønsted acid strength of solid catalyst can be quantitatively measured by various characterisation techniques, while indeed an unambiguously measuring the strength of Lewis acids in a solid is impossible because their sequence may reverse against different probe molecules[65]. Despite of that, Lewis-type superacid sites present in sulfated zirconia was also suggested in literature[66-68], which may enhance the catalytic performance of vicinal protonic sites[58]. Moreover, the catalytic activity for model reaction of a solid acid should also be concerned as characterise its overall acid strength[58]. For sulfated nanocomposites and zeolite catalysts, the contradiction between their catalytic activities in this work and their reported similar acid strength clearly reveal some difficulties and uncertainties in measuring solid acid strength, indicating the necessity of an acceptable definition for solid superacid.

DISCUSSION

Our previous work[22] has investigated the formation mechanism of fibrous ZrO_2/Al_2O_3 nanocomposites, and reveals that the tetragonal zirconia nanocrystallites evenly encompass the long bundle of boehmite nanofibres forming a core-shell structure. In this work the sulfation process only inflicts a negligible effect on the fibrous morphology of these nanocomposites with this effect also being minimized by the increase of zirconium coverage.

583 Therefore, these zirconia nanocomposites with hierarchically macro-mesoporous
584 nanostructures successfully develop into a novel class of solid strong acid.
585
586 An interesting result of these as-synthesized nanocomposite catalysts is that their specific
587 surface areas remain constant with Zr molar percentage varying from 2 % to 50 %. This is
588 quite different from the published data, in which it was reported that loading a heavy metal
589 oxide on a porous carrier will result in the significant decrease of specific surface areas for
590 resulting composites, especially, when the concentration of the loading species was high
591 enough to generate some small independant nanocrystallites, where the surface areas would
592 severely decrease under 100 m^2/g. The reason of this phenomenon for traditional porous
593 carrier is presumably that some of nanocrystallites block the orifices of porous materials[69].
594
595 In this work, the zirconium species are loaded on the long bundle of alumina nanofibres
596 composing a fibrous core-shell structure with zirconium species concentrating on the outer-
597 surface of these rod-like nanocomposites. At high Zr percentage, the growth and distribution
598 of tetragonal zirconia nanocrystallites on fibrous cores at elevated temperature spontaneously
599 form a mesoporous layer with pore size from 1 nm to 10 nm rather than plugging the orifices
600 as been observed previously. These small zirconia nanocrystallites can provide a large
601 specific surface area; therefore, in spite of the specific surface reduction caused by
602 overlapping of the interface between zirconia nanocrystallites and alumina nanofibres, the
603 overall surface areas of these nanocomposties will be not significantly decreased even at high
604 loading ratio of heavy metal oxide. Indeed, it is confirmed by our experiments: at low Zr
605 percentage, zirconia species are highly dispersed on the surface of γ-Al_2O_3 in a spontaneous
606 process[70], and the surface area of nanocomposites slightly decreases due to the increase of
607 apparent density, however, with the Zr percentage increasing to that high enough to generate

608 zirconia nanocrystallites, new surface is also generated by the occurrence of tetragonal
609 zirconia nanocrystallites leading to the increase of the surface areas. At this situation, the
610 materials can bear extremely large loading ratios and their surface area and pore size seems to
611 be independently modified. This can provide an effective approach to design a catalyst with a
612 desired nanostructure, for instance, as observed in our previous work[22], the existence of
613 interconnected macroporous framework increase the resistance to sintering of this materials
614 at elevated temperature and minimize the aggregation of zirconia nanocrystallites, and should
615 also efficiently transport guest molecules to the reactive sites. Therefore, the core shell
616 structure of nanocomposite catalysts and their fibrous morphology are emphasized to be
617 important for catalytic application. As for this reaction, the catalytic performance is mainly
618 determined by acid strength and surface area of as-synthesized nanocomposites with no
619 evidence showed that the pore size and porous framework exerted any effect on the catalytic
620 performance. Since all of nanocomposites catalysts possess similar surface areas, it is easy to
621 conclude the relationship between the acid strength and catalytic activity is such that the
622 pristine sulfated alumina nanofibres only contributes to lower activity; and that the increase
623 in Zr concentration gradually increases the relative acid strength. Consequently, an increase
624 in the catalytic activity of benzoylation of toluene was observed. It is worth mentioning that
625 the acidity for the sample with 30 % Zr molar percentage is slightly weaker than that of
626 pristine sulfated zirconia, but compared with pristine sulfated zirconia, this sample possesses
627 larger surface area which is 154 m^2g^{-1}(reference catalyst is only 88 m^2g^{-1}). The smaller
628 tetragonal nanocrystals of about 3.9 nm attached on alumina nanofibres can generate more
629 eligible active sites for this catalytic reaction. Above this Zr molar percentage, the
630 nanocomposite exhibits higher catalytic activity because the enhancement of acid strength.

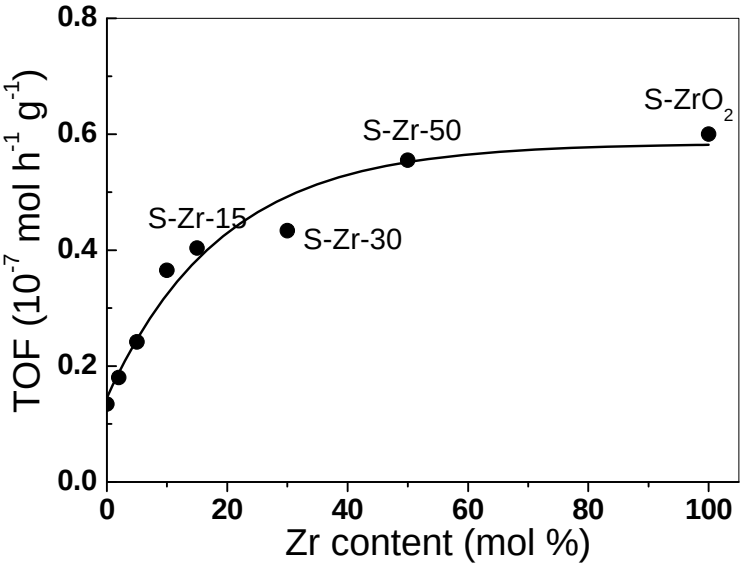

631

632 **Figure 12.** Turnover frequencies of sulfated catalysts as a function of zirconia content

633

634 Moreover, the turnover frequencies of samples including pristine surfated zirconia and
635 fibrous sulfated nanocomposites are calculated based on their surface areas, and plotted as a
636 function of zirconia contents. The catalytic activity of per square meter for S-Zr-50 is very
637 similar to sulfated pristine zirconia, even slightly lower than the pristine sample. This
638 possibly due to the fact that even alumina is a promoter for the sulfated zirconia it mainly
639 enhances the acid sites with intermediate acid strengths rather than very strong acid sites
640 needed by the reaction of benzoylation of toluene. Therefore, the higher catalytic activity of
641 core shell nanocomposites is derived from the higher accessibility of acid sites of smaller
642 tetragonal zirconia nanocrystallites rather than from higher acid strength.

643 **CONCLUSIONS**

644 A series of sulfated ZrO_2/Al_2O_3 nanocomposites with fibrous morphology were synthesized
645 as new solid acid catalyst. The zirconium molar percentage was from 2 % to 50 %. Zr species
646 is highly dispersed on alumina nanofibres at Zr molar percentage up to 5 % and transferred
647 into tetragonal zirconia nanocrystallites above 10 %. Due to the core-shell structure, the
648 surface Zr/Al molar ratios calculated from XPS results are higher than the bulk ratios when

649 Zr molar percentage is above 15 %, and which is about 3 times as much as bulk value at 50 %
650 of Zr molar percentage, suggesting an unambiguous core-shell structure formed. NMR results
651 show that the interaction between zirconia species and alumina strongly correlates with
652 pentacoordinated aluminium sites, which can also be detected by the dislocation of the bond
653 energy 3d of the zirconium.
654
655 The relative acidity of the obtained fibrous sulfated core-shell nanocomposites increases
656 with Zr molar percentage, but the samples maintain an almost constant, large specific surface
657 area due to their unique nanostructure. Benzolyation of toluene is investigated using these
658 novel strong solid acids. It is found that the catalytic activity of the catalyst is strongly related
659 to the surface acidity of the catalyst. The amount of tetragonal zirconia and the resultant
660 relative acidity of the catalyst increase with increasing Zr molar percentage. The sample with
661 50 % of zirconium molar percentage possesses the highest surface acidity equalled to the
662 pristine sulfated zirconia as well as the highest catalytic performance. The catalytic activity of
663 as-synthesized nanocomposites with 30 % zirconium molar percentage surpasses that of the
664 pristine sulfated zirconia due to the synergetic effect of the acid strength and enlargement of
665 surface area.
666
667 **ACKNOWLEDGEMENTS**
668 The financial and infra-structure support from the Queensland University of Technology
669 Chemistry Discipline is gratefully acknowledged. E.M.L is thankful for a Queensland
670 University of Technology doctoral scholarship. One author (WM) is grateful for the financial
671 support in the form of an Australia Post-Doctoral Fellowship Provided by the Australian
672 Research Council and a Smart State Fellowship provided by the Queensland State
673 Government.
674

675 **REFERENCE AND NOTES**

676

677 [1] V.C.F. Holm, G.C. Balley, Bartlesville, in: (Ed.)^(Eds.); USA Patent 3,030,599, 1962.
678 [2] M. Hino, S. Kobayashi, K. Arata, J. Am. Chem. Soc. 101 (1979) 6439.
679 [3] B.M. Reddy, M.K. Patil, Chem. Rev. 109 (2009) 2185.
680 [4] A. Corma, Chem. Rev. 95 (1995) 559.
681 [5] M. Hino, K. Arata, Chem. Lett. (1979) 1259.
682 [6] M. Hino, K. Arata, J.Chem.Soc., Chem. Commun. (1979) 1148.
683 [7] J.H. Clark, Acc. Chem. Res. 35 (2002) 791.
684 [8] G. Rothenberg, Catalysis: Concepts and Green Applications. Wiley-VCH Verlag
685 GmbH &Co. KGaA, Weinheim, 2008.
686 [9] D. Farcasiu, J.Q. Li, Appl. Catal., A 175 (1998) 1.
687 [10] F.R. Chen, G. Coudurier, J.F. Joly, J.C. Vedrine, J. Catal. 143 (1993) 616.
688 [11] Y.-y. Huang, B.-y. Zhao, Y.-c. Xie, Appl. Catal. A: Gen. 173 (1998) 27.
689 [12] T. Jin, M. Machida, T. Yamaguchi, K. TAnabe, Inorg. Chem. 23 (1984) 4396.
690 [13] C. Morterra, G. Cerrato, F. Pinna, M. Signoretto, J. Catal. 157 (1995) 109.
691 [14] G. Larsen, E. Lotero, R.D. Parra, L.M. Petkovic, H.S. Silva, S. Raghavan, Appl.
692 Catal. A: Gen. 130 (1995) 213.
693 [15] B. Djuricic, S. Pickering, P. Glaude, D. Mcgarry, P. Tambuyser, J. Mater. Chem. 32
694 (1997) 589.
695 [16] J.R. Sohn, D.H. Seo, Catal. Today 87 (2003) 219.
696 [17] W. Hua, Y. Xia, Y. Yue, Z. Gao, J. Catal. 196 (2000) 104.
697 [18] Z. Gao, Y. Xia, W. Hua, C. Miao, Top. Catal. 6 (1998) 101.
698 [19] S.Y. Kim, N. Lohitharn, J.G.G. Jr., R. Olindo, F. Pinna, P. Canton, Catal. Commun. 7
699 (2006) 209.
700 [20] P. Canton, R. Olindo, F. Pinna, G. Strukul, P. Riello, M. Meneghetti, G. Cerrato, C.
701 Morterra, A. Benedetti, Chem. Mater. 13 (2001) 1634.
702 [21] J. Zhao, Y. Yue, W. Hua, Z. Gao, Catal. Lett. 116 (2007) 27.
703 [22] E. Liu. Synthesis of one dimensional nanocomposites based on alumina nanofibres
704 and their catalytic applications. Phd thesis, Queensland Unversity of Technology, Brisbane,
705 2011.
706 [23] P. Laidlaw, D. Bethell, S.M. Brown, G.J. Hutchings, J. Mol. Catal. A 174 (2001) 187.
707 [24] A. Heidekum, M.A. Harmer, W.F. Hoelderich, J. Catal. 188 (1999) 230.
708 [25] G.D. Yadav, N.S. Asthana, V.S. Kamble, Appl. Catal. A: Gen. 240 (2003) 53.
709 [26] K. Arata, H. Nakamura, M. Shouji, Appl. Catal. A: Gen. 197 (2000) 213.
710 [27] S.C. Shen, W.K. Ng, Q. Chen, X.T. Zeng, M.Z. Chew, R.B.H. Tan, J. Nanosci.
711 Nanotechno. 7 (2007) 2726.
712 [28] M. Hino, K. Arata, J. Chem. Soc., Chem. Commum. 1985 (1985) 112.
713 [29] J.T. Kloprogge, R.L. Frost, Phys. Chem. Chem. Phys. 1 (1999) 1641.
714 [30] S. Moreau, M. Gervais, A. Douy, Solid State Ionics 101-103 (1997) 625.
715 [31] M.L. Guzman-Castillo, E. Lopez-Salinas, J.J. Fripiat, J. Sanchez-Valente, F.
716 Hernandez-Beltran, A. Rodriguez-Hernandez, J. Navarrete-Bolanos, J. Catal. 220 (2003) 317.
717 [32] S.C. Shen, Q. Chen, P.S. Chow, G.H. Tan, X.T. Zeng, Z. Wang, R.B.H. Tan, J. Phys.
718 Chem. C 111 (2007) 700.
719 [33] R. Iwamoto, C. Fernandez, J.P. Amoureux, J. Grimblot, J. Phys. Chem. B 102 (1998)
720 4342.
721 [34] S.A. Bagshaw, T.J. Pinnavaia, Angew. Chem. Int. Ed. 35 (1996) 1102.

[35] M.K. Younes, A. Ghorbel, J. Sol-Gel Sci. Techn. 26 (2003) 677.
[36] C.J. Dalmaschio, V.R. Mastelaro, P. Nascente, J. Bettini, J.L. Zotin, E. Longo, E.R. Leite, J. Colloid and Interface Sci. 343 (2010) 256.
[37] S.J. Gregg, K.S.W. Sing, in: (Ed.)^(Eds.)Adsorption, Surface Area and Porosity; Academic Press, London, 1982, p 111.
[38] K.S.W. Sing, D.H. Everett, R.A.W. Haul, L. Moscou, R.A. Pierotti, J. Rouquerol, T. Siemieniewska, Pure & Appl. Chem. 57 (1985) 603.
[39] K.S.W. Sing, R.T. Williams, Adsorpt. Sci. Technol. 22 (2004) 773.
[40] J.C. Groen, L.A.A. Peffer, J. Perez-Ramirez, Micropor. Mesopor. Mater. 60 (2003) 1.
[41] G. Li, W. Li, M. Zhang, K. Tao, Catal. Today 93-95 (2004) 595.
[42] R.J. Gillespie, Acc. Chem. Res. 1 (1968) 202.
[43] B. Umansky, J. Engelhardt, W.K. Hall, J. Catal. 127 (1991) 128.
[44] D. Farcasiu, A. Ghenciu, J.Q. Li, J. Catal. 158 (1996) 116.
[45] B.S. Umansky, W.K. Hall, J. Catal. 124 (1990) 97.
[46] T. Riemer, D. Spielbauer, M. Hunger, G.A.H. Mekhemer, H. Knozinger, J. Chem. Soc., Chem. Commum. 1994 (1994) 1181.
[47] A. Corma, V. Fornes, M.I. Juan-Rajadell, J.M.L. Nieto, Appl. Catal. A: Gen. 116 (1994) 151.
[48] J.S. Lee, D.S. Park, J. Catal. 120 (1989) 46.
[49] E.C. Sikabwe, M.A. Coelho, D.E. Resasco, R.L. White, Catal. Lett. 34 (1995) 23.
[50] C. Morterra, G. Cerrato, Phys. Chem. Chem. Phys. 1 (1999) 2825.
[51] H. Yu, H. Fang, H. Zhang, B. Li, F. Deng, Catal. Commun. 10 (2009) 920.
[52] G. Yaluris, R.B. Larson, J.M. Kobe, M.R. Gonzalez, K.B. Fogash, J.A. Dumesic, J. Catal. 158 (1996) 336.
[53] R.S. Drago, N. Kob, J. Phys. Chem. B 101 (1997) 3360.
[54] J.C. Vartuli, J.G. Santiesteban, P. Traverso, N. Cardona-Martinez, C.D. Chang, S.A. Stevenson, J. Catal. 187 (1999) 131.
[55] V. Adeeva, J.W.d. Haan, J. Janchen, G.D. Lei, V. Schunemann, L.J.M.v.d. Ven, W.M.H. Sachtler, R.A.v. Santen, J. Catal. 151 (1995) 364.
[56] F. Babou, G. Coudurier, J.C. Vedrine, J. Catal. 152 (1995) 341.
[57] E.E. Platero, M.P. Mentruit, C.O. Arean, A. Zecchina, J. Catal. 162 (1996) 268.
[58] M.R. Guisnet, Acc. Chem. Res. 23 (1990) 392.
[59] J. Sommer, R. Jost, Pure & Appl. Chem. 72 (2000) 2309.
[60] N. Katada, T. Tsubaki, M. Niwa, Appl. Catal. A: Gen. 340 (2008) 76.
[61] T. Jin, T. Yamaguchi, K. Tanabe, J. Phys. Chem. 90 (1986) 4794.
[62] G.D. Zhou, in: (Ed.)^(Eds.)Inorganic and Structural Chemistry; Kexue Press, Beijing, 1982, p 286.
[63] S.M. Auerbach, K.A. Carrado, P.K. Dutta, Handbook of zeolite science and technology. Marcel Dekker, Inc., New York, 2003.
[64] Y. Xia, W. Hua, Z. Gao, Catal. Lett. 55 (1998) 101.
[65] G.A. Olah, G.K.S. Prakash, A. Molnar, J. Sommer, Superacid Chemistry. John Wiley& Sons, Inc., Hoboken, New Jersey, 2009.
[66] N. Katada, J.-i. Endo, K.-i. Notsu, N. Yasunobu, N. Naito, M. Niwa, J. Phys. Chem. B 104 (2000) 10321.
[67] F.R. Chen, G. Coudurier, J.-F. Joly, J. Vedrine, J. Catal. 143 (1993) 616.
[68] C. Morterra, G. Cerrato, F. Pinna, M. Signoretto, G. Strukul, J. Catal. 149 (1994) 181.
[69] H. Rotter, M.V. Landau, M. Carrera, D. Goldfarb, M. Herskowitz, Appl. Catal. B: Environ. 47 (2004) 111.
[70] Y.-C. Xie, Y.-Q. Tang, Advances in Catalysis. Academic Press, New York, 1990.

772